

Fulde-Ferrell Pairing instability in Spin-Orbit Coupled Fermi Gas

Lin Dong¹, Lei Jiang², and Han Pu¹

¹Department of Physics and Astronomy, and Rice Quantum Institute, Rice University, Houston, TX 77251, USA

²Joint Quantum Institute, University of Maryland and National Institute of Standards and Technology, Gaithersburg, Maryland 20899, USA

Abstract. We consider finite-momentum pairing of superfluid phase in ultracold Fermi gas with spin-orbit coupling when subjected to an effective Zeeman field. Based on our two body and mean field many body calculations, we show that the Fulde-Ferrell type superfluid dominates in zero and finite temperature phase diagram. We examine the origin and properties of this novel phase systematically.

PACS numbers: 05.30.Fk, 03.75.Hh, 03.75.Ss, 67.85.-d

Submitted to: *New J. Phys.*

Keywords: Fermi gas, spin-orbit coupling, Fulde-Ferrell superfluid

1. Introduction

The nature and origin of fermionic pairing was first elucidated in the pioneering work by Bardeen, Cooper, and Schrieffer, widely known as the BCS theory [1]. The attractive pairwise interaction between electrons with opposite spin, albeit extremely weak, can give rise to an instability in normal electron gas towards the formation of zero-momentum Cooper pairs near Fermi surface, and because of pair condensation, ordering of conduction electrons emerge naturally. When subjected to an external Zeeman field, the population balance between electrons with different spins is broken. As a consequence, not all electrons can find a partner to pair up with. If spin-population imbalance is large enough, the pairing of fermions has to occur at finite center-of-mass momentum with deformed Fermi surface state [2]. This exotic possibility of inhomogeneous superfluid was first predicted by Fulde and Ferrell (FF) [3], and Larkin and Ovchinnikov (LO) [4] a little later. FF refers to an order parameter with plane-wave form $\Delta(\mathbf{r}) = \Delta_0 e^{i\mathbf{q}\cdot\mathbf{r}}$, which spontaneously breaks time-reversal symmetry; while LO considers the superfluid with a standing-wave order parameter $\Delta(\mathbf{r}) = \Delta_0 \cos(\mathbf{q}\cdot\mathbf{r})$, which explicitly breaks translational symmetry. Both phases have puzzled the solid-state community for decades in terms of unambiguous experimental evidence to prove their existence. Moreover, the FFLO state is also of interest in quantum chromodynamics at low temperature and high density, where the property of asymptotic freedom may favor color superconductivity [5].

In recent years, due to their exquisite controllability, ultracold atoms have emerged as an ideal platform to simulate real materials. Adjustable interaction and high degrees of control over spin-populations have enabled one with the feasibility to explore this long sought phase. Tremendous theoretical and experimental efforts have been put into optimizing the best detectable parameter regime of FFLO phase. The most promising route is now believed to probe the one-dimensional (1D) spin-imbalanced Fermi gas [6, 7, 8, 9], where indirect evidence of FFLO phase has been found in a recent experiment [10]. However, for 3D Fermi gas, the FFLO phase is not favored [11, 12, 13].

Over the past few years, another milestone achievement in cold atom research is the realization of artificial spin-orbit (SO) coupling, first in bosonic systems [14] and later in fermionic ones [15, 16]. By tailoring the laser fields that generate the SO coupling, various coupling schemes can be realized in principle. It has been realized very recently that, in a Fermi gas, the interplay between the SO coupling and an effective Zeeman field may lead to distortion of single-particle dispersion as well as the Fermi surface, in such a way that finite-momentum dimer state and/or Cooper pairs will be favored [17, 18, 19, 20, 21]. In this work, we provide a unified treatment of both two-body and the many-body physics for a Fermi gas subjected to an isotropic three-dimensional SO coupling (3DSOC) and an effective Zeeman field. The generation of such 3DSOC has been recently proposed by optically dressing four internal atomic states with a tetrahedral geometry [22, 23]. This version of the SO coupling is less explored and unfamiliar to condensed matter community, where 2D Rashba and Dressshaulls SO

couplings are studied extensively. One important advantage of 3DSOC over lower-dimensional SO interaction is that it provides the greatest enhancement of fermionic pairing. Furthermore, due to its isotropic nature, mathematical simplicity is ensured.

The main findings of our work are: i) Under arbitrarily weak Zeeman field, zero-momentum dimer state and conventional BCS superfluid phase are no longer stable. ii) For many-body system, FF state is inherently robust, and ultimately connects to normal phase in a smooth manner as Zeeman field strength is increased, cf. Fig. 3. Moreover, this type of exotic superfluid has different origin in comparison with the previously studied FFLO state. In the absence of the SO coupling, individual particle number with different spins is conserved, hence the imbalance induced finite-momentum pairing has parity symmetry between \mathbf{q} and $-\mathbf{q}$, which should be called LO phase by definition; on the other hand, in the presence of the SO coupling, Zeeman field breaks time-reversal symmetry explicitly and cause the single-particle dispersion to be asymmetric, which underlines the idea of finite-momentum dimer bound state [17] and the FF pairing instability. The center-of-mass momentum of the Cooper pair can be as large as the Fermi momentum. This result should be very encouraging for future experimental exploration.

The rest of the paper is organized as follows. In Sec. 2, we formulate the physical model and introduce the Functional Path Integral technique. We apply this general approach to the system with 3DSOC and discuss our results on two-body physics in Sec. 3 and on many-body physics in Sec. 4. And finally we conclude in Sec. 5.

2. Physical model and general formalism

In this section, we first present the model Hamiltonian under study, and then introduce the widely used functional path integral approach. Using this approach, we can discuss both the two-body physics and the many-body physics at both zero and finite temperatures in a unified way.

2.1. Model Hamiltonian

We start by formulating the Hamiltonian for a non-interacting homogeneous Fermi gas in 3D:

$$\mathcal{H}_0 = \int d\mathbf{r} \psi^\dagger(\mathbf{r}) \left\{ \xi_{\mathbf{k}} + \sum_{i=x,y,z} (v_i k_i + \Lambda_i) \sigma_i \right\} \psi(\mathbf{r}) \quad (1)$$

where $\xi_{\mathbf{k}} = \hbar^2 \mathbf{k}^2 / (2m) - \mu$ and $\psi = [\psi_\uparrow(\mathbf{r}), \psi_\downarrow(\mathbf{r})]^T$ is the fermionic annihilation field operator. We have defined SO coupling strength vector $\mathbf{v} = (v_x, v_y, v_z)$, and the Zeeman field vector $\mathbf{\Lambda} = (\Lambda_x, \Lambda_y, \Lambda_z)$. $\sigma = (\sigma_x, \sigma_y, \sigma_z)$ are Pauli matrices acting on the atomic (pseudo-)spin degrees of freedom. This description is a general model valid for various SO coupling schemes. The single particle spectrum is given by $E^\gamma(\mathbf{k}) = \frac{\hbar^2 \mathbf{k}^2}{2m} + \gamma \sqrt{\sum_i (v_i k_i + \Lambda_i)^2}$ with $\gamma = \pm 1$ denoting the two helicity branches. The experimentally realized [14, 15, 16] equal weight Rashba-Dresselhaus SO coupling

takes the form of Eq. (1) with $\mathbf{v} = (0, 0, \hbar^2 k_r / m)$ and $\mathbf{\Lambda} = (\Omega/2, 0, \delta)$ where k_r is the laser recoil momentum, Ω the Raman laser coupling strength and δ the two-photon detuning. The Rashba SO coupling [25, 26] can be recognized with $\mathbf{v} = (v_x, v_y, 0)$ and $v_x = v_y = \hbar^2 k_r / m$. In our work, we will focus on the 3DSOC [22, 23] with $v_x = v_y = v_z = v$. For this case, due to the isotropic nature of the SO coupling term, the direction of the Zeeman field is irrelevant and we shall choose it to be along the z -axis, and hence $\mathbf{\Lambda} = (0, 0, h)$.

It is important to note that the Zeeman field does induce an asymmetry in the single-particle dispersion relation. To illustrate this, we consider a filled Fermi sea with simple topology (cf. [24]) at zero temperature. In Fig. 1, we plot Fermi surface without and with Zeeman field. In the absence of the Zeeman field, the Fermi surfaces for both helicity branches are represented by spheres centered at zero momentum, as shown in Fig. 1(a). When we turn on the Zeeman field, both Fermi surfaces are distorted and no longer possess reflection symmetry about the $k_z = 0$ plane, as can be clearly seen in Fig. 1(b). In this perspective, the ground state is associated with nonzero total momentum along the k_z -axis.

Next we consider the attractive s -wave contact interaction between un-like spins which, in terms of the creation and annihilation field operators for the original spin states, is represented by

$$\mathcal{H}_{\text{int}} = U_0 \int d\mathbf{r} \psi_{\uparrow}^{\dagger}(\mathbf{r}) \psi_{\downarrow}^{\dagger}(\mathbf{r}) \psi_{\downarrow}(\mathbf{r}) \psi_{\uparrow}(\mathbf{r}) \quad (2)$$

where U_0 is the bare coupling strength to be renormalized using the s -wave scattering length a_s . In this work, we constrain our attention to the experimentally exploited broad Feshbach resonances, which is well captured by the single-channel Hamiltonian prescribed above.

2.2. Functional Path Integral Formalism

In this section, we describe the functional path integral technique [27, 28, 29] and start from the partition function $\mathcal{Z} = \int \mathcal{D}[\psi(\mathbf{r}, \tau), \bar{\psi}(\mathbf{r}, \tau)] \exp \{ -S[\psi(\mathbf{r}, \tau), \bar{\psi}(\mathbf{r}, \tau)] \}$ where the action

$$S[\psi, \bar{\psi}] = \int_0^{\beta} d\tau \left[\int d\mathbf{r} \sum_{\sigma} \bar{\psi}_{\sigma}(\mathbf{r}, \tau) \partial_{\tau} \psi_{\sigma}(\mathbf{r}, \tau) + \mathcal{H}(\psi, \bar{\psi}) \right] \quad (3)$$

is written as an integral over imaginary time τ . Here $\beta = 1/(k_B T)$ is the inverse temperature and $\mathcal{H}(\psi, \bar{\psi})$ is obtained by replacing field operators ψ^{\dagger} and ψ with grassmann variables $\bar{\psi}$ and ψ , respectively. We can integrate out the quartic interaction term using the Hubbard-Stratonovich transformation [29], from which the pairing field $\Delta(\mathbf{r}, \tau)$ is defined. If we assume the mean-field order parameter to be of FF-type $\Delta = \Delta_0 e^{i\mathbf{q} \cdot \mathbf{r}}$, and further integrate out the fermionic fields, we arrive at an effective action as

$$S_{\text{eff}} = \int_0^{\beta} d\tau \int d\mathbf{r} \left(-\frac{|\Delta|^2}{U_0} \right) - \frac{1}{2} \text{Tr} \log[-\mathcal{G}_{\Delta}^{-1}] + \beta \sum_{\mathbf{k}} \frac{\xi_{\mathbf{k}+\mathbf{q}/2} + \xi_{-\mathbf{k}+\mathbf{q}/2}}{2}, \quad (4)$$

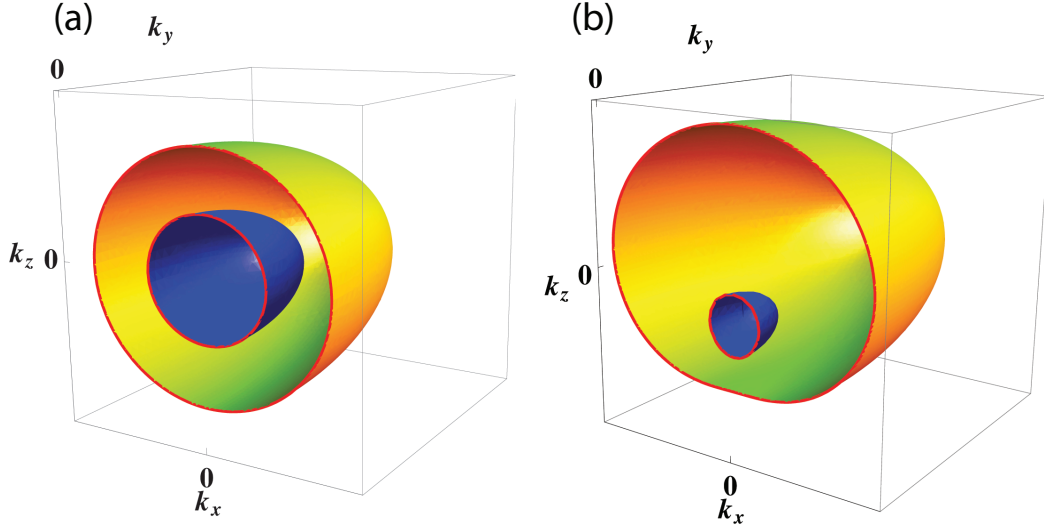


Figure 1. (a) Fermi surfaces (a cut in the $k_y = 0$ plane) in the absence of the Zeeman field. The two concentric Fermi surfaces are spherically symmetric. The inner blue sphere represents the Fermi surface of the $+$ helicity branch, while the outer yellow sphere of the $-$ helicity branch. (b) Fermi surfaces in the presence of the Zeeman field along the z -axis: both Fermi surfaces are deformed in such a way that the cylindrical symmetry about the k_z -axis is still preserved, but the reflection symmetry about the $k_z = 0$ plane is broken.

$$\mathcal{G}_{\Delta}^{-1}(\mathbf{k}, i\omega_m) = \begin{bmatrix} i\omega_m - \xi_{\mathbf{k}+\mathbf{q}/2} - f_+ & i\Delta_0 \hat{\sigma}_y \\ -i\Delta_0 \hat{\sigma}_y & i\omega_m + \xi_{\mathbf{k}-\mathbf{q}/2} - f_- \end{bmatrix} \quad (5)$$

where $f_{\pm} = \sum_i (v_i(k_i \pm \frac{q_i}{2}) \pm \Lambda_i) \sigma_i$. In the second term of Eq. (4), the trace is to be taken over the Nambu spinor space $\Phi(\mathbf{r}, \tau) \equiv [\psi_{\uparrow}, \psi_{\downarrow}, \bar{\psi}_{\uparrow}, \bar{\psi}_{\downarrow}]^T$, the real coordinate space and imaginary time. The last term in Eq. (5) comes from interchanging fermionic fields $\bar{\psi}_{\uparrow}$ and $\bar{\psi}_{\downarrow}$ with ψ_{\uparrow} and ψ_{\downarrow} and the corresponding equal-time limiting procedure [29]. From Eq. (4), we can further sum over Matsubara frequencies to arrive at the grand thermodynamic potential

$$\begin{aligned} \frac{\Omega}{V} = & -\frac{1}{\beta} \ln \mathcal{Z} = -\frac{|\Delta|^2 m}{4\pi \hbar^2 a_s} + \frac{1}{V} \sum_{\mathbf{k}} \left(\frac{\xi_{\mathbf{k}+\mathbf{q}/2} + \xi_{-\mathbf{k}+\mathbf{q}/2}}{2} - \frac{1}{4} \sum_{\alpha=1}^4 |E_{\mathbf{k}}^{\alpha}| \right. \\ & \left. + \frac{|\Delta|^2}{2\epsilon_{\mathbf{k}}} - \frac{1}{2\beta} \sum_{\alpha=1}^4 \ln \left(1 + \exp(-\beta |E_{\mathbf{k}}^{\alpha}|) \right) \right) \end{aligned} \quad (6)$$

where we have regularized the bare interaction strength U_0 in terms of the s -wave scattering length a_s by $\frac{1}{U_0} = \frac{m}{4\pi \hbar^2 a_s} - \frac{1}{V} \sum_{\mathbf{k}} \frac{1}{2\epsilon_{\mathbf{k}}}$. $E_{\mathbf{k}}^{\alpha}$ are the quasi-particle energy dispersion, which are just the four eigenvalues obtained by solving $\det[\mathcal{G}_{\Delta}^{-1}(\mathbf{k}, E_{\mathbf{k}}^{\alpha})] = 0$. In our case, $E_{\mathbf{k}}^{\alpha}$ are too complicated to be analytically presented here.

In the following sections, we restrain our attention to the isotropic 3DSOC with Zeeman field along the z -axis, i.e., $\mathbf{\Lambda} = (0, 0, h)$, and use the ansatz for FF order

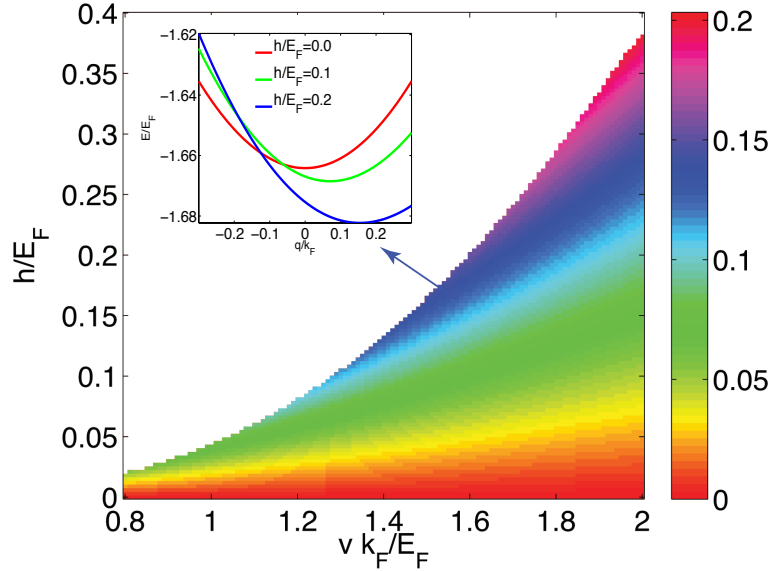


Figure 2. Finite momentum dimer bound state solution for 3DSOC. The coloring shows the magnitude of q_{2b} , varying with the SO coupling strength v and the Zeeman field strength h ; the inset shows bound state energy $E_{\mathbf{q}}$ as a function of q/k_F (along the z -axis) for different h , from top to bottom $h/E_F = 0, 0.1, 0.2$. We fix scattering length as $1/(k_F a_s) = -1$

parameter $\Delta(\mathbf{r}) = \Delta e^{iqz}$.

3. Results on two-body problem

Following the path integral approach, we can characterize two-body properties at low-energy sector by inverse vertex function, which we refer to [30] for more details. We found consistent results reported in our previous paper [17] which are obtained by solving the two-body Schrödinger equation. For a bound-state with total momentum \mathbf{q} , the corresponding energy $E_{\mathbf{q}}$ is obtained by solving the following equation:

$$\frac{m}{4\pi\hbar^2 a_s} = \frac{1}{V} \sum_{\mathbf{k}} \left\{ \frac{1}{\mathcal{E}_{\mathbf{k},\mathbf{q}} - \frac{4v^2}{\mathcal{E}_{\mathbf{k},\mathbf{q}}} \left(\frac{\mathcal{E}_{\mathbf{k},\mathbf{q}}^2}{\mathcal{E}_{\mathbf{k},\mathbf{q}}^2 - (2h + vq)^2} k_{\perp}^2 + k_z^2 \right)} + \frac{1}{2\epsilon_{\mathbf{k}}} \right\} \quad (7)$$

where $\mathcal{E}_{\mathbf{k},\mathbf{q}} = E_{\mathbf{q}} - \epsilon_{\frac{\mathbf{q}}{2}+\mathbf{k}} - \epsilon_{\frac{\mathbf{q}}{2}-\mathbf{k}}$ and $\epsilon_{\mathbf{k}} = \hbar^2 k^2 / (2m)$. For a given set of parameters h , v and a_s , we can numerically obtain the eigenenergy of the dimer bound state $E_{\mathbf{q}}$ as a function of \mathbf{q} . The momentum \mathbf{q}_0 at which $E_{\mathbf{q}}$ reaches the minimum labels the dimer state with lowest energy. The binding energy is defined as $\epsilon_b = 2E_{\min} - E_{\mathbf{q}_0}$, where E_{\min} is the ground state energy of single particle spectrum $E^-(\mathbf{k})$. Only when $\epsilon_b > 0$ can we consider the dimer as a true two-body bound state. Otherwise, its energy lies in the single particle continuum. For the convenience of further comparison with many-body state, here we take the laser recoil momentum k_r , which determines the SO coupling

strength, to be equal to Fermi momentum k_F , which is determined by typical atomic density in experiments [14, 15, 16].

For a Zeeman field along the z -axis, we have $\mathbf{q}_0 = q_{2b}\hat{z}$. Following above-mentioned protocol, we plot q_{2b} as a function of coupling strength and h in Fig. 2. As one would expect, Zeeman field tends to destroy two-body bound state; whereas SO coupling enhances its formation. The competition between these two outlines the critical boundary value, beyond which ϵ_b becomes negative and no stable bound state can be found. With increasing h , the minimum of $E_{\mathbf{q}}$ deviates away from zero momentum to some finite value. As long as Zeeman field is *non-zero*, the lowest-energy bound state would occur at *finite* center-of-mass momentum q_{2b} . Our calculation shows that the magnitude of q_{2b} can be as high as $0.2k_F$.

4. Results on many-body problem

Motivated by the two-body results, one naturally attempts to explore the direct analog for the many-body system, which we study in this section.

We take a canonical ensemble approach by considering a homogeneous system with fixed particle number N and volume V , and hence the density $n = N/V = k_F^3/(3\pi^2)$. The important quantity that determines the mean field phase diagram shall be the free energy, also known as Landau potential, defined as $F = \Omega + \mu N$. At zero temperature, it coincides with the ground state energy. For a given set of parameters (including SO coupling strength v , Zeeman field strength h , interaction parameter $1/(k_F a_s)$, and temperature T), order parameter Δ , chemical potential μ , and the FF momentum $\mathbf{q} = q_{\text{FF}}\hat{z}$ should be determined self-consistently by stationary conditions

$$\frac{\partial F}{\partial \Delta} = 0, \quad \frac{\partial F}{\partial \mu} = 0, \quad \frac{\partial F}{\partial q} = 0. \quad (8)$$

We shall explicitly consider three types of phase: normal gas ($\Delta = 0, q = 0$), BCS state ($\Delta \neq 0, q = 0$), and FF state ($\Delta \neq 0, q_{\text{FF}} \neq 0$).

4.1. Zero-temperature phase diagram on the BCS side

We shall first focus on a relatively weak-interacting regime on the BCS side of crossover and take $1/(k_F a_s) = -1$. In this regime, we can easily justify the mean-field treatment at both zero and finite temperature, and furthermore the SO coupling effect would be more pronounced [34, 35, 36, 37].

To get some insights first, in Fig. 3, we plot free energy as a function of h for a given SO coupling strength $v = E_F/k_F$. (We choose this relatively large SO strength, to avoid possible complications, e.g. Sarma phase [38], phase separation [39] etc.) It is very remarkable to notice that FF state is energetically favored for arbitrarily small h . For instance, at $h = 0.02E_F$, the gain of energy over the BCS pairing phase is $\Delta F = F_{\text{BCS}} - F_{\text{FF}} \approx 4.54588 \times 10^{-5} NE_F$. However, this energy gain quickly increases as h is increased. For example, at $h = 0.28E_F$, we have $\Delta F = 1.13728 \times 10^{-2} NE_F$

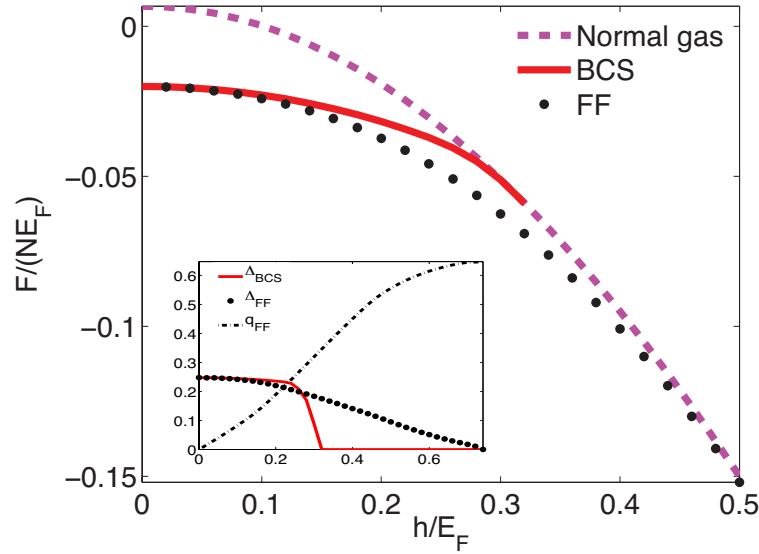


Figure 3. Zero temperature free energy comparison for fixed SO coupling strength $v = E_F/k_F$ and interaction strength $1/k_F a_s = -1$. FF superfluid phase is favored throughout the plotted parameter space. In the inset, we plot the BCS order parameter Δ_{BCS} , the FF order parameter Δ_{FF} (both in units of E_F), and the FF momentum q (in units of k_F) as functions of h .

which is more than two orders of magnitude larger and represents a very large energy value on the BCS side of Feshbach resonance. Once again, the idea of favoring FF phase is backed by the picture of Fermi surface deformation (cf. Fig. 1) and two-body bound state solutions [Eq. (7) and Fig. 2]. When we further increase h , BCS superfluid is taken over by normal phase as the BCS order parameter drops to zero rather sharply (see the inset of Fig. 3); on the other hand, FF state connects to normal phase very smoothly at a much larger value of h .

The FF state here has different origin with the conventional FFLO states in the absence of the SO coupling [6, 7, 8], in which case, for a given interaction strength and with increasing population imbalance (i.e., Zeeman field), one would expect that competitions among various quantum phase (BCS, Sarma, FFLO, and normal phases) could lead to both first- and second-order phase transitions. By contrast in the presence of SO coupling, especially 3DSOC, FF state dominates almost the entire phase diagram, as we map out in the v - h plane Fig. 4(a). The BCS phase only exists on the axis (i.e., in the absence of either the Zeeman field or the SO coupling). Normal phase and FF phase are connected by a smooth boundary, which we identify by setting a threshold value of energy difference $|F_{\text{FF}} - F_{\text{normal}}| \approx 10^{-5} N E_F$. Note that close to the boundary, Δ_{FF} also becomes exceedingly small. For illustration purposes, we schematically added two small regions near $v = 0$, the LO (green) and the phase separation (blue) regions, in the phase diagram. The boundaries of these two phases in the absence of the SO coupling (i.e., at $v = 0$), which are well studied, are obtained from previous results [38, 39, 40].

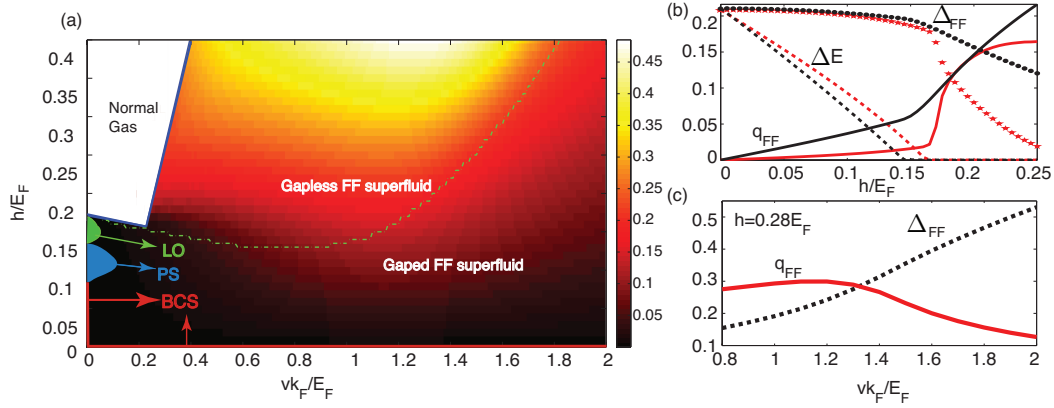


Figure 4. (a) Zero-temperature phase diagram at $1/k_F a_s = -1$ in the parameter space spanned by h and v . The FF phase is divided into gaped and gapless region by the green dashed line. BCS state only exists strictly on the axis marked by two red straight lines. The two blue lines indicate the smooth boundary between FF state and normal phase. Within the FF phase, the color scale indicates the momentum q_{FF} . LO and phase separation (PS) regions are added schematically for illustration purpose. (b) Single-particle excitation gap ΔE , FF order parameter Δ_{FF} and momentum q_{FF} as functions of h . The SO coupling strengths are $v = 0.2E_F/k_F$ (red curves) and $0.5E_F/k_F$ (black curves). (c) Δ_{FF} and q_{FF} as functions of v for $h = 0.28E_F$. In all plots, the energy is in units of E_F , and momentum in units of k_F .

It has been shown that, with increasing SO coupling strength, both these phases are suppressed rather rapidly [40].

Furthermore, in Fig. 4(a), FF phase is divided into the gaped and the gapless regions by examining the single-particle excitation gap $\Delta E = \min\{|E_{\mathbf{k}}^\alpha|\}$, where $E_{\mathbf{k}}^\alpha$ are quasi-particle dispersions introduced in Eq. (6). As shown in Fig. 4(b), ΔE decreases monotonically as a function of h and drops to zero at some critical value of h_c which depends on the SO coupling strength v . The critical value h_c is represented by the green dashed line in Fig. 4(a). At h_c , both q_{FF} and Δ_{FF} exhibit kinks for relatively small SO coupling strength. These kinks get washed out quickly with increasing v (see, for instance, the inset of Fig. 3). On the other hand, in the limit of $v = 0$, these kinks become true jumps signaling the first-order phase transition between the BCS phase and the FF phase region. In Fig. 4(c), we plot q_{FF} and Δ_{FF} as functions of v for a fixed h . We note that even though Δ_{FF} increases monotonically as v , the FF momentum q_{FF} shows non-monotonic behavior: it first increases and then decreases as v is increased from zero.

It is instructive to make comparisons between the two-body results and the many-body results. To this end, we consider a cloud of degenerate Fermi gas typically realized in experiment, with density $n = 10^{12}\text{cm}^{-3}$ which defines k_F and E_F . We compare the two-body dimer momentum q_{2b} with the many-body FF pairing momentum q_{FF} in Fig. 5 at two different values of SO coupling strengths. Note that the range of h values for which the two-body bound state exists is much smaller than that for the existence of

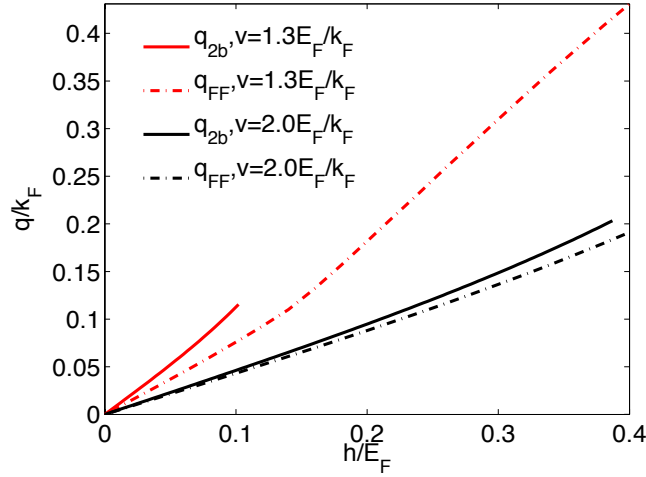


Figure 5. Momentum comparison of the FF state and two-body bound state at $1/k_F a_s = -1$.

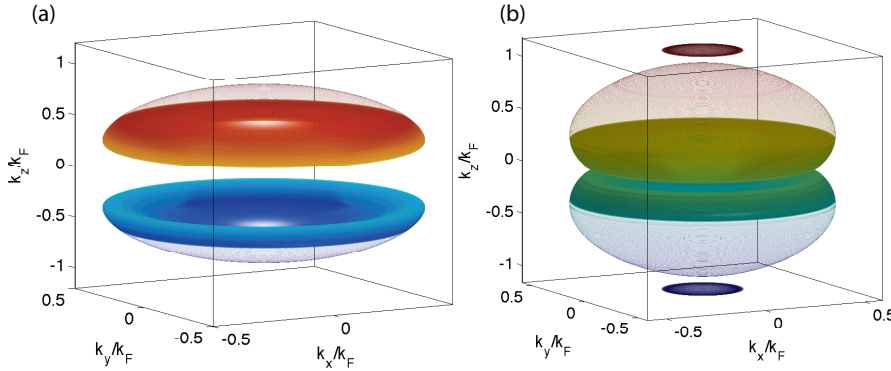


Figure 6. Nodal Fermi surface plots in momentum space. The closed surfaces are formed by momentum values at which the excitation gap ΔE vanishes. Both figures has the same interaction parameter $1/k_F a_s = -1$ as in phase diagram Fig. 3 and coupling strength $v = 0.5E_F/k_F$, while $h = 0.2E_F$ for (a) and $h = 0.35E_F$ for (b).

the FF state. For example, at $v = 1.3E_F/k_F$, two-body bound states only exist for $h < 0.1E_F$; while the FF state extends all the way up to about $h \approx E_F$. As such, the largest q_{FF} that can be achieved is much larger than the largest q_{2b} . In the region where both two-body bound state and the FF state exist, q_{FF} and q_{2b} are comparable, with the latter somewhat larger. The difference between them becomes smaller as the SO coupling strength increases, indicating that at large SO coupling strength, the many-body properties of the system are also dominated by the two-body physics.

Before ending this subsection, we want to remark on the gapless FF state. For Zeeman field strength above the critical value h_c , one or more quasi-particle energy $E_{\mathbf{k}}^\alpha$ will vanish at certain values of momentum \mathbf{k} . Such momenta form closed surfaces (nodal Fermi surface) in momentum space with cylindrical symmetry around the k_z -

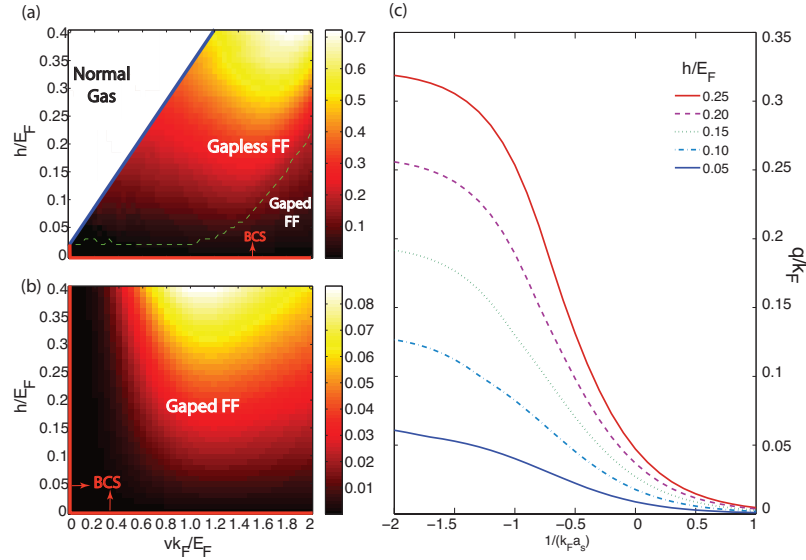


Figure 7. Zero temperature phase diagram with interaction strength $1/k_F a_s = -2$ and $1/k_F a_s = 0$ for (a) and (b), respectively. The color scale represents q_{FF}/k_F . (c) FF superfluid momentum q_{FF} as a function of the interaction strength. For curves from top to bottom, $h/E_F = 0.25, 0.2, 0.15, 0.1, 0.05$, and the SO coupling strength is fixed to be $v = E_F/k_F$.

axis and reflection symmetry about the $k_z = 0$ plane. Hence such nodal Fermi surfaces always appear in pairs and may be measured using the technique of momentum-resolved radio-frequency spectroscopy. Two examples are illustrated in Fig. 6.

4.2. Effects of interaction

So far we have focused on the zero-temperature phase diagram of a weakly-interacting system. Now we briefly discuss the effects of interaction and finite temperature. In Fig. 7(a) and (b), we present two zero-temperature phase diagrams in the h - v plane for $1/k_F a_s = -2$ and 0 , respectively. They are qualitatively similar to the one presented in Fig. 4(a) for $1/k_F a_s = -1$. As we move from the BCS limit towards unitarity, the region for normal phase shrinks and the FF superfluid remains dominant. Furthermore, the region for gaped FF phase increases quickly. At unitarity, the whole parameter space presented in Fig. 7(b) are occupied by the gaped FF phase. On the other hand, for fixed h and v , the FF momentum q_{FF} quickly decreases as we go from the BCS side to the BEC side, as shown in Fig. 7(c). This result is consistent with the one obtained from the two-body study [17, 18].

4.3. Effects of temperature

Finally, we consider the effects of finite temperature. In Fig. 8(a), we plot the phase diagram in the parameter space spanned by h and T by taking $1/(k_F a_s) = -1$ and $v = E_F/k_F$. The FF superfluid phase dominates at small h and low T . There is a

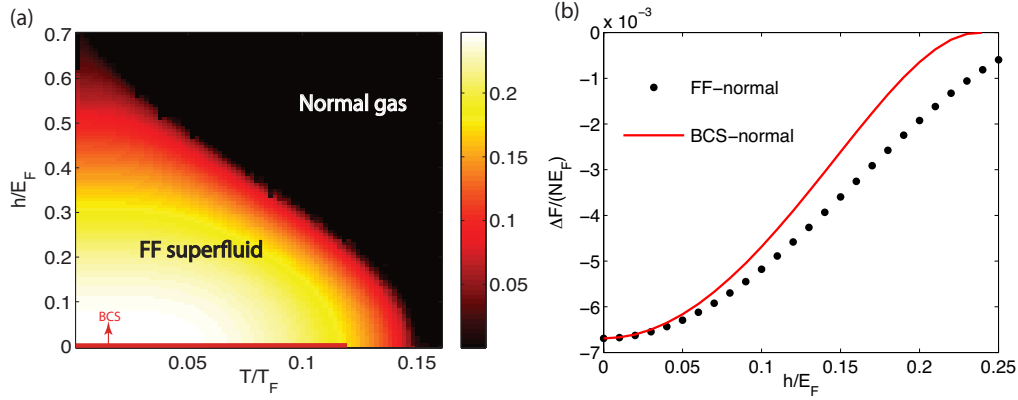


Figure 8. (a) Finite temperature phase diagram at $1/k_F a_s = -1$ and $v = E_F/k_F$. The color scale indicates FF order parameter Δ_{FF} . (b) The free energy difference between the two superfluid phases (BCS and FF) and the normal phase at temperature $T = 0.1T_F$. FF phase always has lowest free energy.

second order transition towards normal phase as h and/or T increases. The BCS phase again only lives on the $h = 0$ axis. In Fig. 8(b), we compare the free energies for all three phases at $T = 0.1T_F$ and clearly show that the FF phase possesses the lowest free energy at any finite values of h as long as h is below a threshold at which the system turns normal.

5. Conclusion

In summary, we have studied spin-orbit coupled Fermi gas subjected to an effective Zeeman field. Based on the picture of Fermi surface deformation, the two-body calculations, and the mean-field many-body results, we conclude that the BCS state with zero-momentum Cooper pairs is not stable against Fulde-Ferrell superfluid pairing at any finite Zeeman field strength. The FF phase is robust against interaction and finite temperature, and the corresponding center-of-mass momentum of the Cooper pair can be comparable to the Fermi momentum.

Acknowledgments

HP is supported by the NSF, the Welch Foundation (Grant No. C-1669), and the DARPA OLE program. We would like to thank Hui Hu and Xia-ji Liu for stimulating discussions, Xiangfa Zhou and Wei Yi for helpful comments, and B. Ramachandhran for the help on improving the quality of some figures.

- [1] J. Bardeen, L.N. Cooper, and J. R. Schrieffer, Phys. Rev. **106**, 162 (1957) and Phys. Rev. **108**, 1175 (1957) .
- [2] Sedrakian, A., Mur-Petit, J., Polls, A. and Muther, H. , Phys. Rev. A **72**, 013613 (2005).
- [3] P. Fulde, and R. A. Ferrell, Phys. Rev. **135**, A550 (1964).
- [4] A. I. Larkin and Y. N. Ovchinnikov, Sov. Phys. JETP **20**, 762 (1965).
- [5] R. Casalbuoni and G. Nardulli, Rev. Mod. Phys. **76**, 263320 (2004).

- [6] G. Orso, Phys. Rev. Lett. **98** 070402 (2007).
- [7] H. Hu, X.-J. Liu, P. D. Drummond, Phys. Rev. Lett. **98** 070403 (2007).
- [8] M. Tezuka, M. Ueda, Phys. Rev. Lett. **100** 010403 (2008) .
- [9] Hong Lu, L. O. Baksmaty, C. J. Bolech, and Han Pu, Phys. Rev. Lett. **108**, 225302 (2012).
- [10] Y.-A. Liao, A. S. C. Rittner, T. Paprotta, W. Li, G. B. Partridge, R. G. Hulet, S. K. Baur, and E. J. Mueller, Nature **467**, 567 (2010).
- [11] M. W. Zwierlein, A. Schirotzek, C. H. Schunck, and W. Ketterle, Science **311**, 492 (2006).
- [12] G. B. Partridge, W. Li, R. I. Kamar, Y.-A. Liao, and R. G. Hulet, Science **311**, 503 (2006).
- [13] M. M. Parish, F. M. Marchetti, A. Lamacraft, and B. D. Simons, Nature Physics **3**, 124 (2007).
- [14] Y.-J. Lin *et al.*, Phys. Rev. Lett. **102**, 130401 (2009); Y.-J. Lin, R. L. Compton, K. Jimenez-Garcia, J. V. Porto and I. B. Spielman, Nature, **426**, 628 (2009); Y.-J. Lin, K. Jimenez-Garcia, and I. B. Spielman, Nature (London) **471**, 83 (2011). Y.-J. Lin, R. L. Compton, K. Jimenez-Garcia, W. D. Phillips, J. V. Porto and I. B. Spielman, Nature Physics, **7**, 531 (2011).
- [15] P. Wang, Z.-Q. Yu, Z. Fu, J. Miao, L. Huang, S. Chai, H. Zhai, and J. Zhang, Phys. Rev. Lett. **109**, 095301 (2012).
- [16] L. W. Cheuk, A. T. Sommer, Z. Hadzibabic, T. Yefsah, W. S. Bakr, and M. W. Zwierlein, Phys. Rev. Lett. **109**, 095302 (2012).
- [17] L. Dong, L. Jiang, H. Hu, and H. Pu, arXiv:1211.1700 (2012).
- [18] V. B. Shenoy, arXiv:1211.1831 (2012).
- [19] Z. Zheng, M. Gong, X. Zou, C. Zhang, and G.-C. Guo, arXiv:1208.2029 (2012) and arXiv:1212.6826 (2012).
- [20] F. Wu, G.-C. Guo, W. Zhang, and W. Yi, arXiv:1211.5780 (2012).
- [21] X.-J. Liu, and H. Hu, arXiv:1302.0553, (2013).
- [22] B. M. Anderson, G. Juzeliunas, V. M. Galitski, and I. B. Spielman, Phys. Rev. Lett. **108**, 235301 (2012).
- [23] Y. Li, X. Zhou, and C. Wu, Phys. Rev. B **85**, 125122 (2012).
- [24] J. P. Vyasankere, S. Zhang, and V. B. Shenoy, Phys. Rev. B **84**, 014512 (2011).
- [25] A. Jacob, P. Ohberg, G. Juzeliunas, L. Santos, Appl. Phys. B. **89**, 439, (2007).
- [26] J. Dalibard, F. Gerbier, G. Juzeliunas, and P. Ohberg, Rev. Mod. Phys. **83**, 1523 (2011).
- [27] C. A. R. S de Melo, M. Randeria, and J. R. Engelbrecht, Phys. Rev. Lett. **71**, 3202 (1993); M. Randeria, in *Bose-Einstein Condensation*, edited by A. Griffin, D. W. Snoke, and S. Stringari, (Cambridge University Press, Cambridge, England, 1995), p. 355-392.
- [28] H. Hu, X.-J. Liu, and P. Drummond, Europhys. Lett. **74**, 574 (2006); R. B. Diener, R. Sensarma, and M. Randeria, Phys. Rev. A **77**, 023626 (2008).
- [29] Henk T. C. Stoof, Koos B. Gubbels, Dennis B.M. Dickerscheid, Ultracold Quantum Fields, Springer, 2009.
- [30] L. Jiang, X.-J. Liu, H. Hu, and H. Pu, Phys. Rev. A **84**, 063618 (2011).
- [31] J.-Y. Zhang, S.-C. Ji, Z. Chen, L. Zhang, Z.-D. Du, B. Yan, G.-S. Pan, B. Zhao, Y.-J. Deng, H. Zhai, S. Chen, and J.-W. Pan, Phys. Rev. Lett. **109**, 115301 (2012).
- [32] B. Ramachandhran, B. Opanchuk, X.-J. Liu, H. Pu, P. D. Drummond, and H. Hu, Phys. Rev. A **85**, 023606 (2012).
- [33] Q. Zhu, C. Zhang, and B. Wu, arXiv:1109.5811, (2011).
- [34] Z.-Q. Yu, and H. Zhai, Phys. Rev. Lett. **107**, 195305 (2011).
- [35] M. Iskin, and A. L. Subasi, Phys. Rev. Lett. **107**, 050402 (2011).
- [36] M. Gong, S. Tewari, and C. Zhang, Phys. Rev. Lett. **107**, 195303 (2011).
- [37] H. Hu, L. Jiang, X.-J. Liu, and H. Pu, Phys. Rev. Lett. **107**, 195304 (2011).
- [38] H. Hu, and X.-J. Liu, Phys. Rev. A **73** 051603(R) (2006).
- [39] D. Sheehy, and L. Radzihovsky, Phys. Rev. B **75**, 136501 (2007).
- [40] R. Liao, Y. Yi-Xiang, and W.M. Liu, Phys. Rev. Lett. **108**, 080406 (2012).